Version: 2008 Oct 27

Trigonometric Parallaxes of Massive Star Forming Regions: I. S 252 & G232.6+1.0

M. J. Reid[1], K. M. Menten[2], A. Brunthaler[2], X. W. Zheng[3], L. Moscadelli[4] and Y. Xu[2,5]

ABSTRACT

We are conducting a large program with the NRAO Very Long Baseline Array (VLBA) to measure trigonometric parallaxes of massive star-forming regions across the Milky Way. Here we report measurement of the parallax and proper motion of methanol masers in S 252 and G232.6+1.0. The parallax of S 252 is 0.476 ± 0.006 mas ($2.10^{+0.027}_{-0.026}$ kpc), placing it in the Perseus spiral arm. The parallax of G232.6+1.0 is 0.596 ± 0.035 mas ($1.68^{+0.11}_{-0.09}$ kpc), placing it between the Carina-Sagittarius and Perseus arms, possibly in a Local (Orion) spur of the Carina-Sagittarius arm. For both sources, kinematic distances are significantly greater than their parallax distances. Our parallaxes and proper motions yield full space motions accurate to ≈ 1 km s^{-1}. Both sources orbit the Galaxy ~ 13 km s^{-1} slower than circular rotation.

Subject headings: techniques: interferometric — astrometry — spiral arm: Perseus, Crux–Scutum — distances — masers — individual (S 252, G232.6+1.0)

1. Introduction

An image of the Milky Way, taken by an observer in another galaxy would probably reveal a spiral structure dotted with many bright HII regions. The Milky Way is believed to be spiral galaxy, and a best "educated guess" is that it is a barred Sb to Sc galaxy

[1]Harvard-Smithsonian Center for Astrophysics, 60 Garden Street, Cambridge, MA 02138, USA

[2]Max-Planck-Institut für Radioastronomie, Auf dem Hügel 69, 53121 Bonn, Germany

[3]Department of Astronomy, Nanjing University Nanjing 210093, China

[4]INAF, Osservatorio Astrofisico di Arcetri, Largo E. Fermi 5, 50125 Firenze, Italy

[5]Purple Mountain Observatory, Chinese Academy of Sciences, Nanjing 210008, China

(Blitz, Fich & Kulkarni 1983; Gerhard 2002). However, since we are inside the Milky Way, it has proved very difficult to properly characterize its structure (Bash 1981; Burton 1988).

Originally, studies of HI emission offered the opportunity to map the structure of the Milky Way (Oort, Kerr & Westerhout 1958). HI emission on longitude-velocity plots clearly demonstrated that there were some coherent, large-scale structures, which were probably spiral arms in the Milky Way. However, determining accurate distances to HI clouds proved problematic, and this made the task of turning longitude-velocity data into a true plan-view of the Milky Way very uncertain (Burton 1988). Later, millimeter-wave observations of molecules, such as CO, also revealed coherent, large-scale structures with higher contrast than seen in HI (Dame, Hartmann & Thaddeus, P. 2001). But, again, uncertain distances to molecular clouds precluded making a true map of the Milky Way with sufficient accuracy map the spiral structure of the Milky Way.

Georgelin & Georgelin (1976) published a "plan-view" model of the spiral structure of the Milky Way. This approach involved combining optical observations of young stars and radio data of HI cloud and HII region emissions. Luminosity distances to nearby stars were used where available and kinematic distances elsewhere, mostly for more distant HII regions. More recently, Taylor & Cordes (1993) have modeled pulsar dispersion measures to refine the Georgelin & Georgelin model. While subject to very significant uncertainties from kinematic distances, the Georgelin & Georgelin model has remained the basis for the "standard" model of the spiral structure of the Milky Way for over 30 years.

The primary goal of our project is to reinforce the foundations of models of the spiral structure of the Milky Way by measuring distances directly to regions of massive star formation across large portions of the Milky Way. This paper is the first (Paper I) in a series, including Papers II through V (Moscadelli et al. 2009; Xu et al. 2009; Zhang et al. 2009; Brunthaler et al. 2009) published in this volume. We are using the NRAO [1] Very Long Baseline Array (VLBA) to determine trigonometric parallaxes of strong methanol maser sources, which are associated with regions of massive star formation and their attendant HII regions. Sampling spiral arms roughly every kpc should determine the true locations of arms, and allow us to use other databases to "interpolate" between the star forming regions measured with masers. With accurate distances to some of the largest star forming regions, we should be able to verify the existence and determine the locations of the postulated Perseus, Carina–Sagittarius, Crux–Scutum, and Norma spiral arms. Ultimately, we hope to extend these measurements with a larger sample, including a similar study in the southern

[1]The National Radio Astronomy Observatory is a facility of the National Science Foundation operated under cooperative agreement by Associated Universities, Inc.

hemisphere, and produce a map of the 3-dimensional structure of bright material associated with massive young stars that defines spiral structure.

In addition to distances, the observations used to determine trigonometric parallaxes yield excellent measurements of secular proper motions, with accuracies of $\approx$ 1 km s^{-1} (Xu et al. 2006a). Combining radial velocity measurements with proper motions (and distances) yields full 3-dimensional velocities, relative to the motion of the Sun. Thus, through this project and other VLBI efforts, notably the Japanese project VERA (Kobayashi et al. 2005), we hope to determine the full kinematics of massive star forming regions in the Milky Way, which will accurately define the rotation curve of the Milky Way and, in turn, its enclosed mass as a function of Galactocentric radius. Finally, we should be able to show how material in spiral arms actually moves, to characterize kinematic anomalies (such as in the Perseus Arm) and, hopefully, to understand why these anomalies occur.

2. Radio Wavelength Parallax Essentials

2.1. Methanol Masers

Methanol (CH_3OH) masers are excellent astrometric targets for parallax measurements. Class II methanol masers (e.g. 6.7 and 12 GHz transitions) are widespread and associated with newly formed stars in regions of high-mass star formation. The masers generally are compact ($\sim$ 1 mas), slow moving, and vary slowly, which minimizes the possibility of brightness variations mimicking position shifts. While the 6.7 GHz masing transition is generally stronger than the 12 GHz transition, there are dozens of 12 GHz sources with peak flux densities $>$ 5 Jy, which is sufficient to serve as a phase-reference for the VLBA. Also, the 12 GHz transition is at a high enough frequency to offer minimal sensitivity to unmodeled ionospheric fluctuations and to minimize interstellar scatter broadening. However, once all 12 GHz masers have been measured, the 6.7 GHz methanol masers will be attractive targets.

We note that 22 GHz H_2O masers are also good astrometric targets; they are compact, strong, widespread, and the high frequency of the transition minimizes ionospheric fluctuations and interstellar scattering problems. However, H_2O masers can be variable on time scales as short as weeks to months and, since parallax observations are best made over a timespan of 1 yr, this can be problematic. Water masers are generally associated with high-velocity outflows from young stellar objects. Since, for well-planned measurements, parallax and proper motion are essentially uncorrelated, parallax estimates should not be affected by the magnitude of the proper motion. However, one of the most astrophyscially interesting by-products of maser astrometry is the determination of the full space-motions of the asso-

ciated young stellar objects. If there are fast internal motions, then one needs to understand details of the outflows in order to transform from measured maser motions to a frame tied to the central stellar object. The accuracy of this transformation is typically better than a few km s^{-1} for slowly expanding methanol masers (Xu et al. 2006a), but can be of order 10 km s^{-1} for the rapidly expanding H_2O masers (Hachisuka et al. 2006).

2.2. Identifying Background Reference Sources

Since astrometric accuracy is enhanced by finding background sources (ie, QSOs) as close in angle to the maser sources as possible, we first conducted surveys for background sources near potential maser targets. Using the sustainable recording rate of 128 Mbits s^{-1} of the VLBA in 2006 (which is being substantially upgraded), we are able to use background sources as weak as a few mJy. We identified candidate background sources by selecting all sources in the NRAO VLA Sky Survey (NVSS) that were nearly unresolved (at $\approx 40''$ resolution) and within $\approx 1.5^\circ$ of a maser target. Typically we found ≈ 30 candidates stronger than ≈ 20 mJy for any maser target. These candidate sources were observed in snap-shot mode with the VLA at 8 and 15 GHz to determine a spectral index and further test compactness. Candidates that remained unresolved with these observations and displayed a synchrotron spectral index are likely to be extragalactic and have compact cores that can be imaged with VLBA observations. Typically we find between 1 and 3 suitable QSOs within about 1.5 degrees of a target methanol maser source (Xu et al. 2006b). When possible we re-observed with these sources with the VLA A- or B-configurations to determine absolute positions to better than 30 mas.

2.3. Atmospheric Delay Calibration

The main source of systematic error for cm-wave phase-referenced observations is uncompensated interferometric delays introduced by the Earth's atmosphere and ionosphere. The model used in the VLBA correlator is a seasonally-averaged calculation that does not take into account variations in atmospheric pressure, total water-vapor content, nor the delay induced by the ionosphere. At a frequency of 12 GHz the correlator model will typically be in error by about 0.2 to 0.4 nsec of delay, corresponding to 5 to 10 cm of excess path length, for sources at high elevation angles. Substantial gains in reducing systematic errors owing to atmospheric mis-modeling can be obtained by directly measuring and removing these effects.

For the last decade, we have been working to understand better our sources of systematic error and to find methods of correcting our data for these errors (Reid et al. 1999; Reid & Brunthaler 2004) Currently, we use observations of extragalactic sources spread over the sky to measure broad-band delays. For sources with well determined positions (better than 1 mas), residual delays measured by the VLBA will be dominated by the effects of atmospheric mis-modeling. Typically, we observe ≈ 15 such sources over a range of source azimuths and elevations in rapid succession over a time span of about 40 min.

The choice of sources and the observing sequence were determined by computer code with the following procedure: We generated a candidate source list starting with the ICRF catalog (Fey et al. 2004) and keeping only the 60 sources that had been observed > 1000 times, had coordinate uncertainties < 1 mas, and had little structure at 8 GHz (i.e. structural indexes of 1 or 2). Trial schedules were generated by randomly skipping though the candidate source list; we required that a source was above an elevation of 8° at a minimum of 6 VLBA stations and that no station missed more than a total of 5 sources. For each trial schedule, we generated fake data and performed a least-squares fit solving for zenith atmospheric delays and clock offsets for all stations. We generally examined 1000 trial schedules and chose the one that minimized the largest of the formal zenith delay uncertainties among the 10 stations.

We placed these "geodetic" blocks before the start, in the middle, and after the end of our phase-reference observations, in order to monitor slow changes in the total atmospheric delay for each telescope. The data were taken in left circular polarization with eight 4-MHz bands that spanned 480 MHz of bandwidth between 12.10 and 12.58 GHz; the bands were spaced in a "minimum redundancy configuration" to uniformly sample, as best as possible, all frequency differences. This was accomplished with bands spaced by 0, 1, 4, 9, 15, 22, 32 and 34 times 14 MHz. The data were correlated, corrected for ionospheric delays using total electron content measurements (Walker & Chatterjee 2000), and residual multi-band delays and fringe rates were determined for all sources.

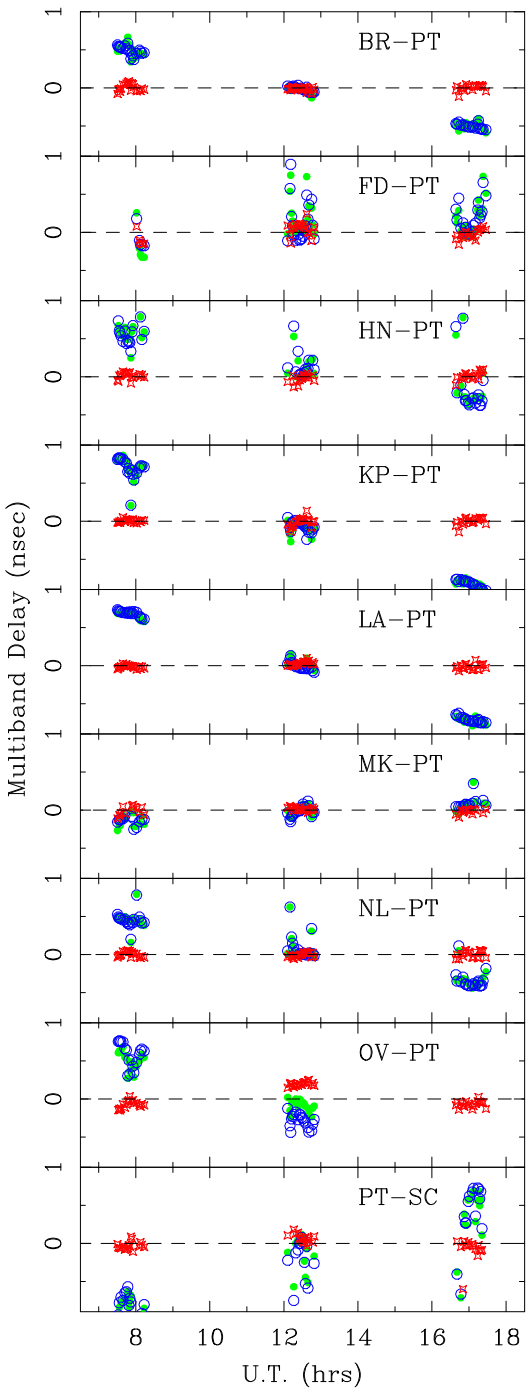

Fig. 1.— Data (green dots), model (blue circles), and residuals (red crosses) for multi-band delays from a solution to all three geodetic blocks simultaneously. Only residuals for baselines involving the reference antenna (PT) are plotted; standard VLBA 2-character antenna names indicate the interferometer baseline. For each antenna, we solved for a vertical atmospheric delay and its time derivative and, except for the reference antenna, a clock and its time derivative. NB: 0.1 nsec $\approx$ 3 cm of path delay.

The multi-band delays and fringe rates were modeled as owing to a vertical atmospheric delay and delay-rate, as well as a clock offset and clock drift rate, at each antenna. Owing to the short (1 min) integration times, the fringe rates are fairly uncertain and the multi-band delays carry most of the weight in the solutions. In order to protect the fitting process from occasional bad data, we used an iterative approach that down-weights outliers relative to the previous solution. Specifically, after each iteration, the uncertainty assigned to the each delay or fringe rate datum was increased by a factor of $\exp[(r/4)^2]$, where r is the post-fit residual divided by the original uncertainty. This procedure heavily down-weights $> 4\sigma$ outliers. Typically, only a few percent of the input data were significantly down-weighted. Sample data, model, and residuals from our first epoch observations are shown in Fig. 1.

In some cases, the delay residuals indicated departures from the linear (in time) model; an example can be seen in the non-zero mean delay residuals (*red crosses*) in Fig. 1 for the interferometer baseline formed by VLBA antennas OV and PT. We believe this is due to unusually large, quasi-random, changes in the zenith delay at antenna 8 during this observation. In order to improve the calibration, we then solved for zenith delays and clock offsets for each 40-min block separately. Calibration of the phase-referencing data was done by linearly interpolating between these three solutions.

Using our least-squares fitting program, we estimated zenith atmospheric path-delays with accuracies typically < 1.0 cm ($< 0.4\lambda$). Independent comparisons of our technique with those using Global Positioning System (GPS) data and an image-optimization approach confirm this accuracy (Honma, Tamura & Reid 2008). Correction for atmospheric delays results in significant improvement in relative position accuracy, compared to observations that rely solely on the VLBA correlator model. Finally, using more than one background reference source, at different offsets and position angles with respect to the target maser source, when phase-referencing further reduces sensitivity to any residual systematic errors from atmospheric mis-modeling.

2.4. Absolute Positions

When conducting phase-referenced observations, it is important that the position of the reference source is well determined (Beasley & Conway 1995). A position error, $\Delta\theta_{err}$, for the reference source results in residual phases shifts that are sinusoidal with a 24 hour period and an amplitude of $\sim \Delta\theta_{err}/\theta_f$ turns, where θ_f is the interferometer fringe spacing. When applied to a target source, offset from the reference source by θ_{sep}, the reference phases can no longer be perfectly modeled as a position shift (at the position of the target source). This results in a second-order position shift of $\sim \Delta\theta_{err}\theta_{sep}$, as well a degradation of the imaging.

While the second-order position shift, in principle, can be constant from epoch to epoch and not affect a parallax measurement, the image degradation can be serious and even preclude detection of a weak source.

We attempted to determine the absolute positions of our sources to better than 10 mas accuracy. The 12 GHz methanol masers for which we sought to measure parallaxes contain some bright, compact spots that serve as good astrometric targets. Since we used strong maser signals as the phase reference, in order to allow the detection of weak background sources close in angle on the sky, we needed to measure the maser positions. Because the 12 GHz methanol masers are often spread over a region of $\sim 1''$, we had to determine their positions from our VLBA data. We accomplished this in one of two ways. If one of the background sources had a well determined position (< 10 mas) and we could image it after phase referencing to the maser (even with a poorly determined *a priori* maser position), then we iteratively refined the maser position to a similar accuracy.

When the maser position cannot be measured against a known source by phase referencing, one can take advantage of the excellent correlator model and map of a strong maser spot by simply Fourier transforming the data, following amplitude calibration and atmospheric model correction, but *without* phase referencing (i.e. after Calibration "step 3" describe in §3.3). This produces a very crude image, which resembles optical speckles, owing to the large phase excursions introduced mostly by short-term fluctuations in the atmospheric delay. For our data, the brighter speckles were concentrated in a region of about 50 to 100 mas radius, and we were able to estimate the centroid of the speckle distribution to an accuracy of about 10 to 20 mas.

Table 1 lists the absolute positions the maser and background continuum sources, as well as the observed brightness and restoring beam sizes at the first epoch.

3. Observations and Data Analysis

3.1. Observations

Our observations were conducted under VLBA program BR100B. We observed S 252 and G232.6+1.0 over 8-hour tracks at four epochs: 2005 October 13, 2006 April 6 and October 4, and 2007 March 25. These dates well sample the peaks of the sinusoidal trigonometric parallax signature in right ascension. The declination signature is significantly smaller than that for right ascension, and we made no effort to detect it. This sampling provides maximum sensitivity for parallax detection and ensures that we can separate the secular proper motion (caused by projections of Galactic rotation, as well as any peculiar motion of the masers and

Table 1. Positions and Brightnesses

Source	R.A. (J2000) (h m s)	Dec. (J2000) (d ' ")	$\theta_{\rm sep}$ (deg)	P.A. (deg)	T_b (Jy/b)	$V_{\rm LSR}$ (km s^{-1})
S 252.....	06 08 53.3395	+21 38 29.100	...	...	$6-15$	10.8
J0603+2159 ...	06 03 51.55708	+21 59 37.6982	1.2	-73	0.080	...
J0607+2129 ...	06 07 59.5657	+21 29 43.720	0.3	-125	0.005	...
J0607+2218 ...	06 07 17.4360	+22 18 19.080	0.5	-132	0.008	...
J0608+2229 ...	06 08 34.3109	+22 29 42.981	0.2	-153	0.056	...
G232.6+1.0.....	07 32 09.7833	-16 58 12.589	...	...	$3-7$	22.8
J0735$-$1735 ...	07 35 45.81246	-17 35 48.5027	1.1	126	0.29	...
J0729$-$1636 ...	07 29 23.93	-16 36 56.2	0.8	-62	...	...

Note. — Absolute positions are accurate to about ±1 mas and are based on the positions of the ICRF catalog sources J0603+2159 and J0735–1735, whose positions are known to about ±0.5 mas in each coordinate. Angular offsets ($\theta_{\rm sep}$) and position angles (P.A.) east of north relative to the maser source are indicated in columns 4 and 5. Brightnesses (T_b) for the background sources are from the first epoch. Restoring beam sizes (FWHM) were 1.0 mas (round) for S 252 and its background calibrators and 8.0×2.8 mas^2 at a P.A. of 15° east of north for G232.6+1.0and its calibrators.

the Sun) from the sinusoidal parallax effect.

For S 252 we observed four background sources, while for G232.6+1.0 we observed two background sources. Table 1 lists the positions of these sources. We alternated between two ≈ 20 min blocks, each consisting of observations of a maser target and its background sources. Within a block, we switched sources every 40 s, typically achieving 30 s of on-source data. The observing sequence for the S 252 block was four repetitions of S 252, J0607+2129, S 252, J0607+2218, S 252, J0608+2229, S 252, J0603+2159. A similar sequence was used for the G232.6+1.0 block; however, with only two background sources, we used eight repetitions of such a cycle. We used the methanol maser as the phase-reference source, because it is considerably stronger than the background sources and could be detected on individual baselines in the available on-source time.

We placed observations of two strong sources (J0530+1331 and J0555+3948) near the beginning, middle and end of the observations in order to monitor delay and electronic phase differences among the IF bands. In practice, however, we found minimal drifts and used only a single scan for this calibration. We also used data from these strong sources to check the variations in phase across the bandpasses and found them to vary by $< 5^\circ$ across the central 90% of the band. Since the masers were observed near band center and we discarded the outer channels for the continuum sources, we made no bandpass corrections.

The rapid-switching observations employed four adjacent frequency bands of 4 MHz bandwidth and recorded both right and left circularly polarized signals. The four (dual-polarized) bands were centered at Local Standard of Rest velocities ($V_{\rm LSR}$) of 108.54, 10.00, -88.54 and -187.08 km s^{-1} for S 252, and at 120.54, 22.00, -76.54 and -175.08 km s^{-1} for G232.6+1.0. For both sources, the masers were contained in the second band.

3.2. Correlation of Recorded VLBA Data

The raw data recorded on tape (or more recently on transportable disks) at each antenna were shipped to the VLBA correlation facility in Socorro, NM. The data from individual antenna pairs were cross-correlated with an integration time of 0.92 sec. Integration times were kept short to allow position shifting of the data to accommodate a priori uncertainties in the maser positions. At this integration time, we could not process all eight frequency bands in one pass with sufficient spectral resolution for the maser band, without exceeding the maximum correlator output rate. Thus, we correlated the data in two passes. One pass was processed with 16 spectral channels for each of the eight frequency bands. This data was used for the geodetic blocks (to determine atmospheric delays and clock drifts)

and for the background continuum sources observed in rapid-switching (phase-referencing) mode. Another pass was processed with 256 spectral channels, but only for the single (dual-polarized) frequency band containing the maser signals, giving a velocity resolution of 0.38 km s^{-1}, assuming a rest frequency of 12178.597 MHz for the $2_0 \rightarrow 3_{-1}$ E transition of methanol.

3.3. Calibration

We calibrated the correlated data using the NRAO Astronomical Image Processing System (AIPS). The calibration sequence included four steps. Step 1 involved correction of interferometer delays and phases for the effects of diurnal feed rotation (parallactic angle), for errors in the values of the Earth's orientation parameters used at the time of correlation, and for any small position shifts in the a priori coordinates of either the maser or background sources. Since the VLBA correlator model includes no ionospheric delays, we used global total electron content models to remove ionospheric effects. At this point, we also corrected the data for residual zenith atmospheric delays and clock drifts (determined from the geodetic block data).

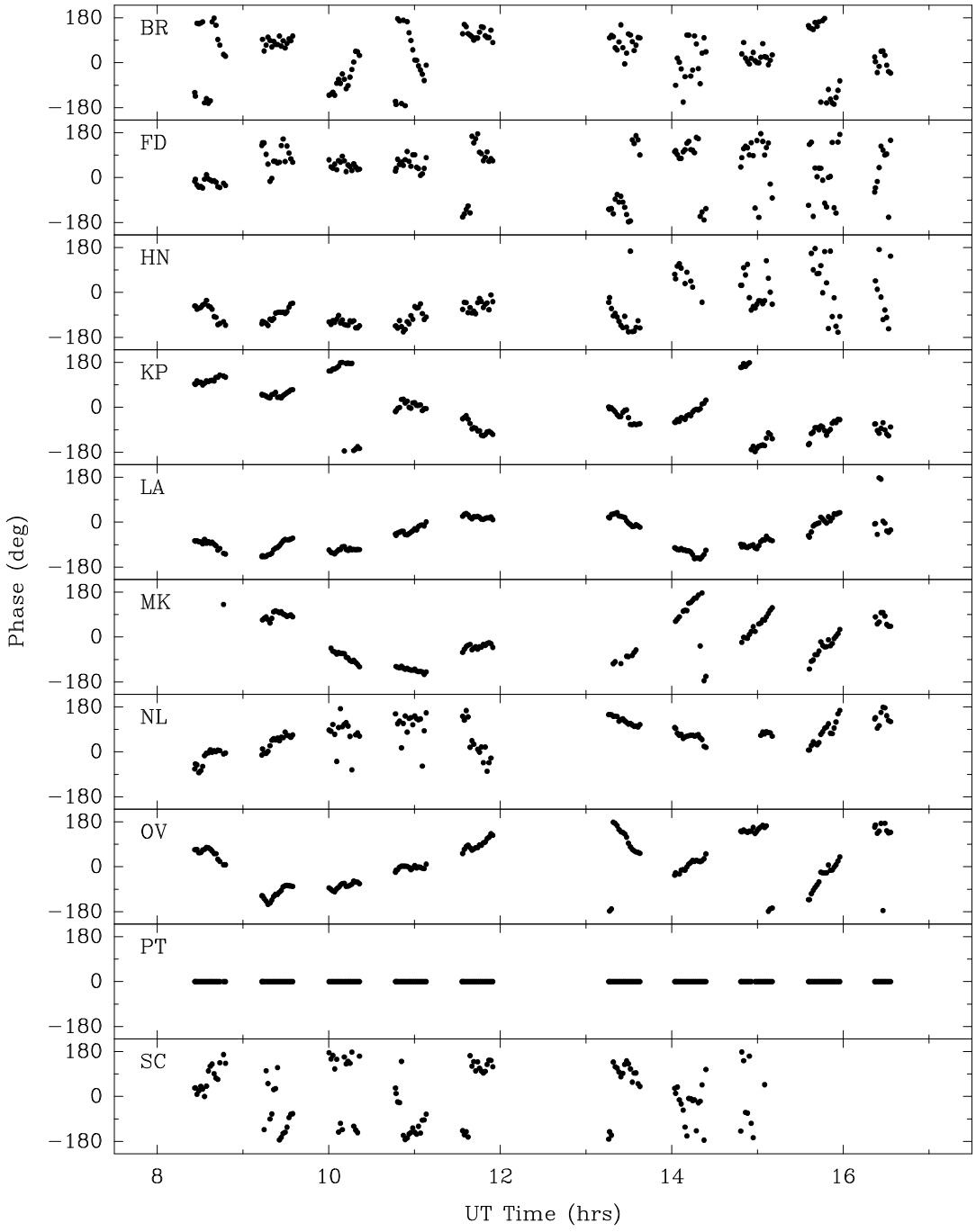

Fig. 2.— Antenna-based phases from maser emission of S 252 at $V_{\rm LSR} = 11.8$ km s^{-1} used to phase reference both the maser and background continuum source interferometer data. These data were taken from the first epoch observations on 2005 Oct 13. VLBA antennas are labeled in the upper left corner of each panel. Interferometer phases are defined between $-180°$ and $+180°$ and wrap across these boundaries. For most antennas at most times, the phase is contained within a few cycles, indicating calibration of interferometer elements to within a few wavelengths. Where the baseline phases, constructed from these antenna phases, exhibited jumps greater than 60°, we flagged the data between them on a baseline by baseline basis.

In step 2 we adjusted interferometer visibility amplitudes for the small (few %) effects of biases in the threshold levels of the data samplers at each station. We also entered system temperature and antenna gain curve information into calibration tables, which allow conversion of correlation coefficients to flux density units.

In step 3, we performed a "manual phase-calibration" to remove delay and phase differences among all eight 4-MHz bands. This was done by selecting one scan on a strong calibrator, fitting fringe patterns to the data for each frequency band, and then shifting delays and phases to remove offsets. At this point, the interferometer data had delay errors less than ≈ 0.03 nsec (≈ 1 cm of excess path) for sources observed at high elevations. Finally, we shifted the frequency axes of the maser interferometer spectra to compensate for the Doppler shift caused by changing projection of the Earth's orbit and spin toward the source, in order to keep a constant $V_{\rm LSR}$ in any given spectral channel.

After step 3, the visibility phases are calibrated for all known effects and residual phases are typically dominated by short-term atmospheric variations of ~ 3 cm and nearly constant absolute position errors usually less than ~ 3 mas (see §2.4 and Table 1). Atmospheric variations cancel, to first order in the source separations (typically 1° or 0.02 radians on the sky), when constructing phase differences ("phase-referencing") between the target maser and the background continuum source. Absolute position errors are largely constant over our observations and cancel over time when fitting for a parallax. (Only the time-variable position changes, owing to parallax and proper motion, will not cancel in time. Typical Galactic proper motions of ≈ 1 mas y^{-1} result in differential position shifts of typically 0.02 mas, when the galactic source (e.g. maser) is used as the phase reference.)

The final calibration, step 4, involved selecting a maser phase-reference. We used a single spectral channel of the maser source, selected to be strong on the longest interferometer baselines, and hence compact. The reference phases from spectral channel 128 at $V_{\rm LSR} = 10.8$ km s^{-1} of S 252 are shown in Fig. 2. The flux density of this maser was typically ~ 10 Jy. For most antennas at most times the phases were easily "connected" and interpolated to the time of the background source observations. (There was one background source observation between each pair of S 252 phase-reference observations.) When the differences between adjacent reference phases exceeded 60°, the data between those times was discarded. The limit of 60° was chosen to be large enough to allow for (calibratable) short-term atmospheric fluctuations, but not too large so as to encounter turn ambiguities when interpolating between reference phases. Note that this editing was done on baseline (not antenna) phases, since baseline phases are what are ultimately used when calibrating data.

For G232.6+1.0, the sole strong maser feature presented as a asymmetric double with

the strongest component having a flux density of $\sim$ 5 Jy (see inset in Fig. 6). Using this spectral channel as a phase reference initially resulted in the appearance of a false double-structure in the background continuum source image. To remedy this problem, we performed an iterative self-calibration sequence on the maser channel in order to construct a good image of that maser double. We then used this image to remove the effects of the maser structure when calculating reference phase tables.

4. Parallax and Proper Motion Fitting

After calibration, we Fourier transformed the gridded *(u,v)*-data, using the AIPS task IMAGR, to make images of the maser emission in all spectral channels and the background continuum sources. The images were deconvolved with the point-source response using the CLEAN algorithm. In order to provide the data needed to measure parallax and proper motions, we fitted an elliptical Gaussian brightness distribution to the brightest maser spots and the background continuum sources at all four epochs, using the task JMFIT. In general, our background sources are compact and appear dominated by a single component. The (generally weak) extragalactic continuum sources we find usually are very compact and have little internal structure that could complicate astrometric accuracy. This is in contrast to well known quasars with bright jets, such as superluminal sources, for which structural changes would be problematic.

The change in position of the maser spot(s) relative to the background continuum source(s) was then modeled by the parallax sinusoid in both coordinates, completely determined by one parameter (the parallax) and a secular proper motion in each coordinate. The model included the effects of the ellipticity of the Earth's orbit.

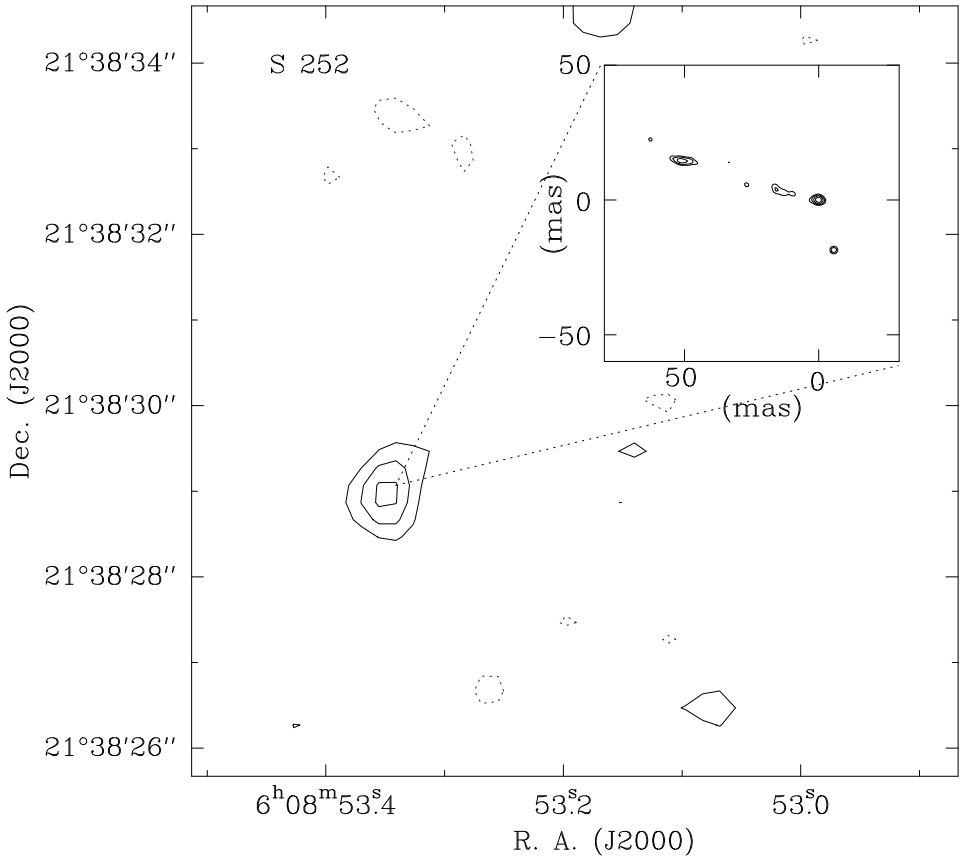

Fig. 3.— Image of continuum emission associated with a hyper-compact HII region in S 252, generated from archival VLA data, with the velocity-integrated maser emission inset. The reference maser spot is at the origin of the inset. Maser spots used for the parallax fits are at $(0, 0)$ and $(-5, -18)$ mas. Contour levels are linearly spaced at 0.08 mJy for the HII region, and they start at 3 Jy km s^{-1} and increase by factors of 2 for the maser emission. Zero contours are suppressed for clarity.

The choice of data and their weighting in the parallax and proper motion fitting is complicated by two issues. Firstly, some maser spots are blended in position and frequency and the intensity of the blended components can vary with time. Generally, we fitted positions in all spectral channels where the maser spots looked to be good candidates for astrometry (i.e. compact emission, minimal blending, etc.). We then fitted a parallax and proper motion to each spot separately in order to assess its astrometric quality, based on the magnitude of the post-fit residuals. Usually only a small number of maser spots were passed along for final fitting. Secondly, the formal position uncertainties were often unrealistically small, since (a priori unknown) sources of systematic error often dominate over random noise.

The north-south components of relative positions often have greater uncertainty than the east-west components, because (1) interferometer beams are generally larger in the north-south direction and (2) systematic errors from unmodeled atmospheric delays usually are more strongly correlated with north-south positions (Honma, Tamura & Reid 2008). In order to allow for such systematic errors, we assigned independent "error floors" to the east-west and north-south position data and added these floors in quadrature with the formal position-fitting uncertainties. Trial parallax and proper motion fits were conducted and a separate reduced χ^2 (per degree of freedom) statistic was calculated for the east-west and north-south residuals. The error floors were then adjusted iteratively so as to make the reduced $\chi^2 \approx 1.0$ for each coordinate.

Individual maser spots were allowed to have different proper motions, owing to internal motions that are typically a few km s^{-1} for 12-GHz methanol masers. However, since we expect no detectable proper motion for the extragalactic sources, in the cases where we had more than one extragalactic source, we constrained the proper motion of any given maser spot to be the same when measured against all extragalactic sources. Note that we used a single east-west and north-south error floor in any least-square fit and these floors are the same for the combined and the individual fits. The small differences in error floors among the fits can result in the combined fit parameters differing slightly from a simple combination of the individual fit values.

4.1. S 252

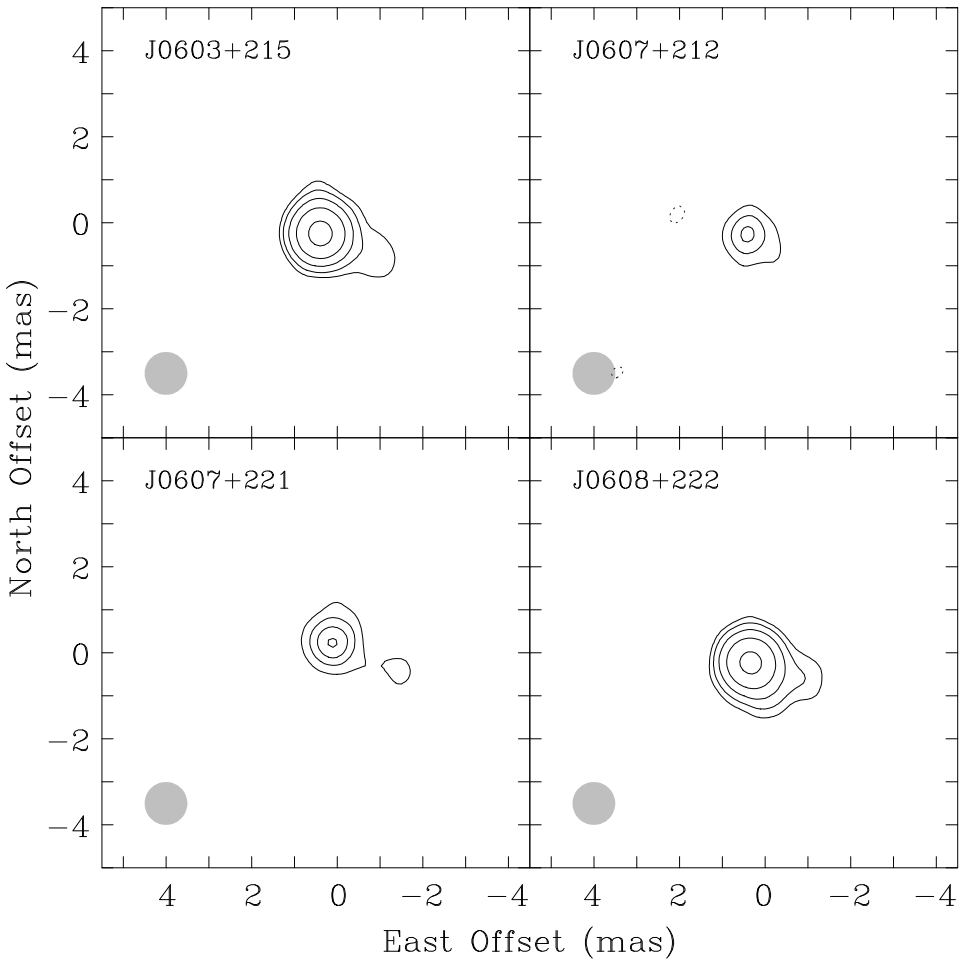

Fig. 4.— Images of background continuum sources near S 252. Source names are in the upper left corner and restoring beams are in the lower left corner of each panel. All images are from the first epoch observations on 2005 Oct 13. For the stronger sources, contour levels are spaced by factors of 2, starting at 4 mJy for J0603+2159 and 3 mJy for J0608+2229. For the weaker sources, contour levels are spaced linearly at 1.5 mJy increments for J0607+2129 and 2 mJy for J0607+2218. Zero contours are suppressed for clarity. The weakest source, J0607+2218, was not used for the parallax measurement of S 252.

For the S 252 sources, the interferometer ("dirty") beam had a FWHM of 1.3 by 0.6 mas at a PA of -5° East of North. In the deconvolution ("CLEAN") step, we used a round restoring beam of 1.0 mas in order to simplify the fitting of potentially close maser spots.

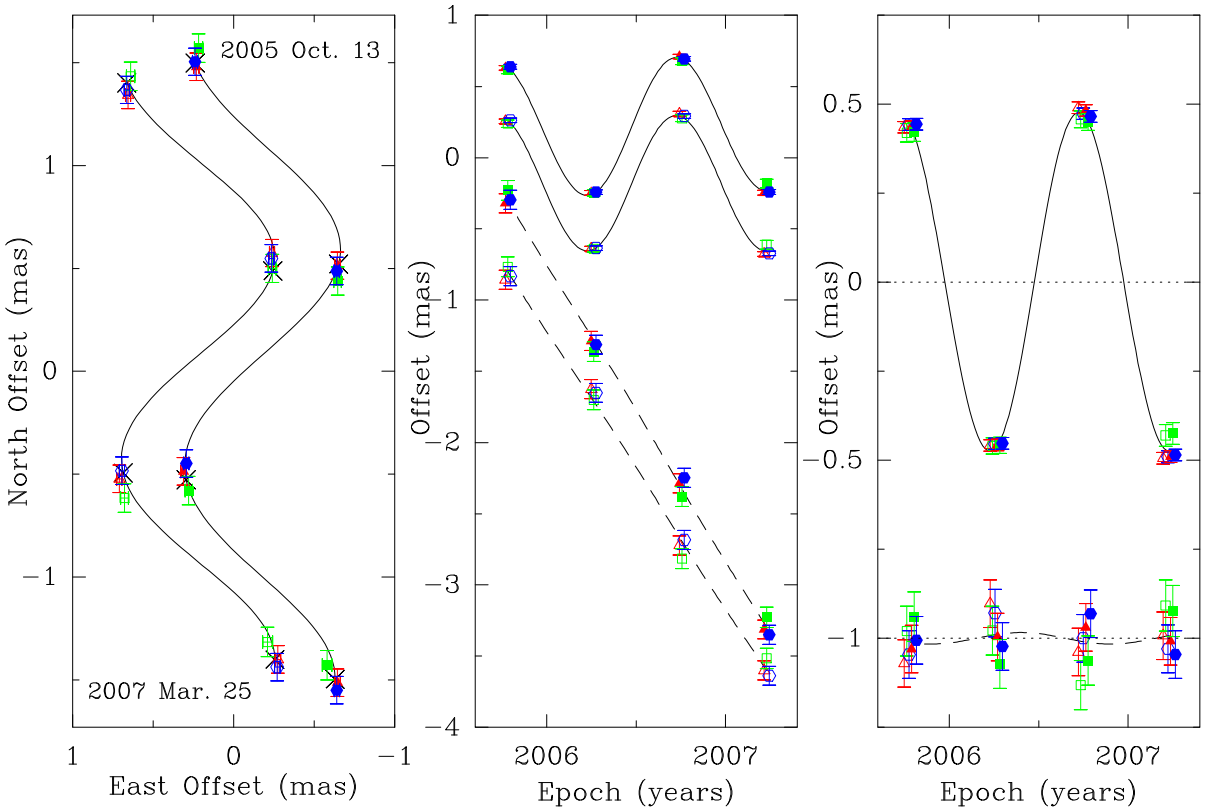

Fig. 5.— Parallax and proper motion data and fits for S 252. Plotted are position measurements of two maser spots *(open and solid symbols)* relative to the three background sources: J0603+2159 *(red triangles)*, J0607+2218 *(green squares)* and J0608+2229 *(blue hexagons)*. *Left Panel:* Positions on the sky with first and last epochs labeled. Data for the two maser spots are offset horizontally for clarity. The expected positions from the parallax and proper motion fit are indicated *(crosses)*. *Middle Panel:* East *(solid lines)* and North *(dashed lines)* position offsets and best fit parallax and proper motions fits versus time. Data for the two maser spots are offset vertically, the northward data have been offset from the eastward data, and small time shifts have been added to the data for clarity *Right Panel:* Same as the *middle panel*, except the with the best fit proper motions have been removed, allowing all data to be overlaid and the effects of only the parallax seen.

In Fig. 3, we show VLA archive data of 8.4 GHz continuum emission from an associated hyper-compact HII region, with the first epoch image of the maser emission integrated over all spectral channels with detectable emission. In Fig. 4, we show an image at the first epoch of the four background radio sources. The small departures from a point-like image at the lowest contour levels is probably a result of small imperfections in the phase calibration transfered from the maser data.

The position data from three of the four background continuum sources produced consistent results with small residuals. The data for J0607+2129, our weakest source, yielded significantly larger post-fit residual and was not used for the final parallax and proper motion fitting. The fitting results are presented in Table 2. Our measured parallax for S 252 is 0.476 ± 0.006 mas; the quoted uncertainty is the formal error multiplied by $\sqrt{2}$ to allow for the possibility of correlated position variations for the two maser spots. This could result from small variations in the background source or from unmodeled atmospheric delays, both of which would affect the two maser spots nearly identically.

Our parallax for S 252 corresponds to a distance of $2.10^{+0.027}_{-0.026}$ kpc. The average proper motion of the two astrometric maser spots is 0.02 ± 0.01 mas y^{-1} toward the East and -2.02 ± 0.04 mas y^{-1} toward the North. At the distance implied by the parallax measurement, these motions correspond to 0.3 km s^{-1} and -20.1 km s^{-1} eastward and northward, respectively. Completing the full space velocity, the average LSR velocity of the spots is 11.2 km s^{-1}, which corresponds to a heliocentric radial velocity of 23.6 km s^{-1}. The space motion of the two masers spots are almost identical, and, since internal motions of methanol masers are typically small (Moscadelli et al. 2002), we expect the maser space motions to follow that of the central young stellar object to within about ± 3 km s^{-1}.

4.2. G232.6+1.0

Table 2. S 252 Parallax & Proper Motion Fits

Maser $V_{\rm LSR}$ (km s^{-1})	Background Source	Parallax (mas)	μ_x (mas y^{-1})	μ_y (mas y^{-1})
10.8	J0603+2159	0.485 ± 0.016	$+0.00 \pm 0.03$	-1.94 ± 0.10
10.8	J0607+2218	0.462 ± 0.012	$+0.03 \pm 0.02$	-1.95 ± 0.14
10.8	J0608+2229	0.477 ± 0.009	-0.01 ± 0.02	-1.96 ± 0.07
11.5	J0603+2159	0.481 ± 0.013	$+0.03 \pm 0.02$	-2.07 ± 0.04
11.5	J0607+2218	0.459 ± 0.012	$+0.06 \pm 0.02$	-2.08 ± 0.13
11.5	J0608+2229	0.473 ± 0.009	$+0.02 \pm 0.01$	-2.10 ± 0.09
10.8	combined	0.476 ± 0.006	$+0.00 \pm 0.01$	-1.95 ± 0.04
11.5			$+0.03 \pm 0.01$	-2.08 ± 0.04

Note. — Combined fit used a single parallax parameter for both maser spots relative to the three background sources; a single proper motion was fit for each maser spot relative to all three background sources. The quoted uncertainty for the combined parallax fit is the formal fitting uncertainty multiplied by $\sqrt{2}$ to allow for the possibility of correlated positions for the 2 maser spots.

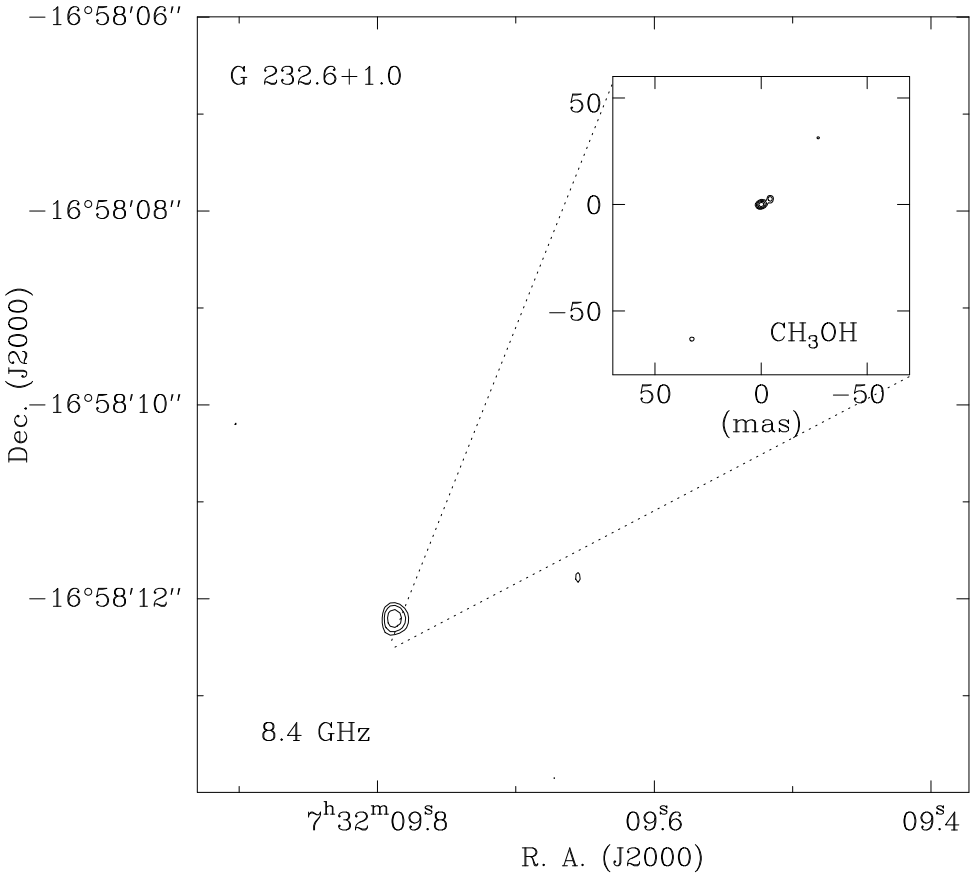

Fig. 6.— Image of continuum emission associated with a hyper-compact HII region in G232.6+1.0, generated from archival VLA data, with the velocity-integrated maser emission inset. The reference maser spot is at the origin of the inset and was the only spot used for the parallax fits. Contour levels start at 0.55 mJy and increase by factors of 1.4 for the HII region, and they start at 0.33 Jy km s^{-1} and increase by factors of 2 for the maser emission. Zero contours are suppressed for clarity.

For G232.6+1.0, the reference maser spot was considerably larger than in S 252, and we could only effectively use the inner five VLBA stations for imaging. The dirty beam was about 8 by 3 mas at a PA of 15°. Because of the limited interferometer data for this low Declination source, we used a restoring beam equal to the FWHM of the dirty beam.

In Fig. 7, we show an image from the first epoch of of the background radio source J0735-1735. The second background source observed, J0729-1636, was not detected. We plot the position of the $V_{\rm LSR}$ =22.8 km s^{-1} maser spot relative to J0735-1735 in Fig. 8.

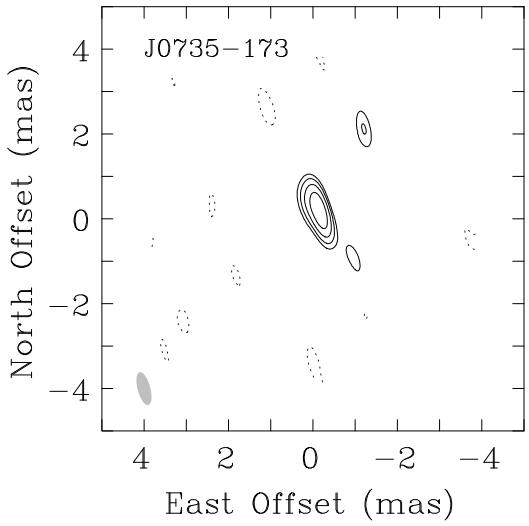

Fig. 7.— Image of background continuum source, J0735-1735, used for the parallax measurements of G232.6+1.0. The image is from the first epoch observations on 2005 Oct 13. The restoring beam (*gray*) is in the lower left corner. Contour levels are spaced by factors of 2, starting at 20 mJy. The zero contour is suppressed for clarity.

Our measured parallax for G232.6+1.0 is 0.596 ± 0.035 mas, which corresponds to a distance of $1.68^{+0.11}_{-0.09}$ kpc. The proper motion of the single maser spot is -2.17 ± 0.06 toward the East and 2.09 ± 0.46 mas toward the North. For the measured parallax, the proper motions correspond to -17 km s^{-1} and $+17$ km s^{-1} eastward and northward, respectively.

Unlike for S 252, where we had multiple spots and background sources, for G232.6+1.0 we found only one maser and one background source suitable for astrometric measurements. The VLBA calibrator survey shows that in 2002 at 8.6 GHz the background source, J0735–1735, had a second component of ≈ 0.05 Jy beam^{-1} separated by ≈ 4 mas at a position angle of $\approx 40^\circ$ east of north from the strongest component of ≈ 0.20 Jy beam^{-1}. At 12.2 GHz we found J0735–1735 to be dominated by a single component with peak brightnesses of 0.29, 0.24, 0.31 and 0.32 Jy beam^{-1} at our four epochs. The apparent variations in brightness are small and consistent with a nearly constant brightness source that is imaged in the presence of typical calibration errors, especially variable phase-referencing coherence losses at different epochs.

In light of the potential limitations of a single background source and a single maser spot, and because there was effectively only one degree of freedom in the fit, which is dominated by the east-west data, we have doubled the formal uncertainties as a precaution. Table 3 summarizes the parameters of the parallax and proper motion fits.

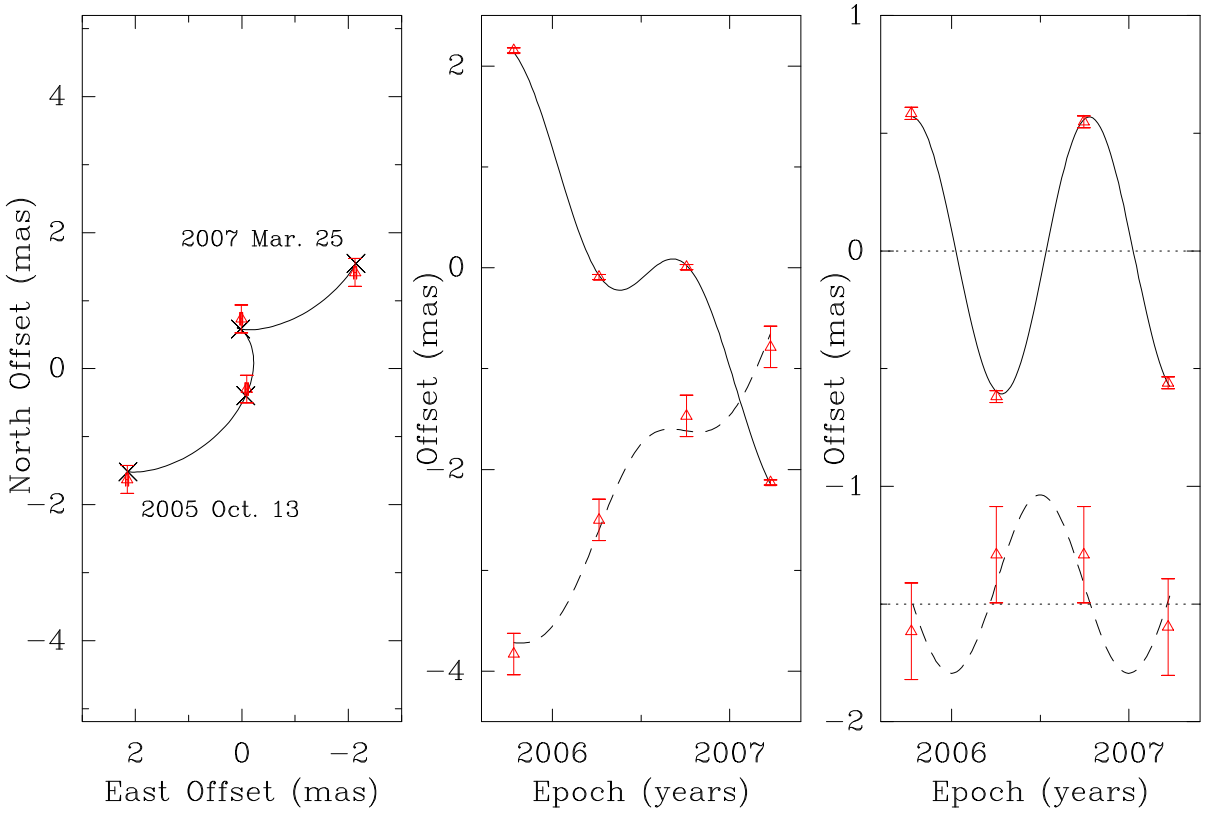

Fig. 8.— Parallax and proper motion data and fits for G232.6+1.0. Plotted are position measurements of the most compact maser spot relative to the background source J0735-1735 *(red triangles)*. *Left Panel:* Positions on the sky with first and last epochs labeled. The expected positions from the parallax and proper motion fit are indicated *(crosses)*. *Middle Panel:* East *(solid lines)* and North *(dashed lines)* position offsets and best fit parallax and proper motions fit versus time. The northward data have been offset from the eastward data for clarity. *Right Panel:* Same as the *middle panel*, except the with the best fit proper motion has been removed, allowing the effects of only the parallax seen.

5. Galactic 3-D Motions

In order to study the 3-dimensional motion of the maser sources in the Galaxy, we need to convert their radial and proper motions from the equatorial heliocentric reference frame in which they are measured into a Galactic reference frame. A convenient Galactic frame is one rotating with a circular velocity $\Theta(R)$ at the position of the source: ie, a "local standard of rest" at the location of maser. We will describe this procedure in detail in Reid et al. (in preparation, Paper VI).

Conversion to a rotating Galactic reference frame depends upon several parameter values. The IAU standard value for the distance of the Sun to the Galactic center is $R_0 = 8.5$ kpc and for the rotation speed of the LSR is $\Theta_0 = 220$ km s^{-1}. We assume a flat rotation curve, i.e. $\Theta(R) = \Theta_0$. (The effects of a non-flat rotation curve will be considered Paper VI.) Finally, we use the Solar Motion values $U_\odot = 10.0 \pm 0.4$, $V_\odot = 5.2 \pm 0.6$ and $W_\odot = 7.2 \pm 0.4$ km s^{-1}, derived from Hipparcos data by Dehnen & Binney (1998). For these parameter values, our parallax, $V_{\rm LSR}$ and proper motion results for S 252 imply "peculiar motions" (relative to circular motion) of -4 ± 3 km s^{-1} toward the Galactic center, -16 ± 1 km s^{-1} in the direction of Galactic rotation, and -2 ± 1 km s^{-1} toward the North Galactic Pole. For G232.6+1.0 we find peculiar motion components of of -4 ± 3 km s^{-1} toward the Galactic center, -10 ± 3 km s^{-1} in the direction of Galactic rotation, and 0 ± 2 km s^{-1} toward the North Galactic Pole. Thus, both sources are orbiting the Galaxy slower than it spins (i.e. slower than circular rotation).

We note that evidence from proper motion of Sgr A*, the super-massive black hole at the center of the Galaxy, strongly suggests that $\Theta_0/R_0 = 29.5$ km s^{-1} kpc^{-1}, with an uncertainty less than 1% (Reid & Brunthaler 2004). Thus, were we to adopt $R_0 = 8.0$ kpc (Reid 1993), this would require $\Theta_0 = 236$ km s^{-1}. For these Galactic parameters, the peculiar velocity components change only slightly: for S 252 they become -3 km s^{-1} toward the Galactic center, -16 km s^{-1} in the direction of Galactic rotation, and -2 km s^{-1} toward the North Galactic Pole, and for G232.6+1.0 they become 0 km s^{-1} toward the Galactic center, -10 km s^{-1} in the direction of Galactic rotation, and 0 km s^{-1} toward the North Galactic Pole. Thus, changing R_0 and Θ_0 by amounts consistent with current levels of uncertainty would not change the conclusion that these star forming regions orbit the Galaxy slower than it spins.

Research on the structure of the Galaxy in Nanjing University is supported by the National Science Foundation of China under grants 10133020, 10103003 and 10373025, and A. Brunthaler is supported by DFG Priority Programme 1177.

Table 3. G232.6+1.0 Parallax & Proper Motion Fit

Maser $V_{\rm LSR}$ (km s^{-1})	Background Source	Parallax (mas)	μ_x (mas y^{-1})	μ_y (mas y^{-1})
22.8	J0735–1735	0.596 ± 0.035	-2.17 ± 0.06	$+2.09 \pm 0.46$

Note. — We conservatively quote uncertainties that are double the formal fitting values, since effectively there is only one degree of freedom for the parallax and proper motion solution which is dominated by the east-west data.

REFERENCES

Bash, F. N., 1981, ApJ, 250, 551

Beasley, A. J.& Conway, J. E. 1995, ASPC, 82, 328

Blitz, L., Fich, M., Kulkarni, S. 1983, *Science*, 220, 1233

Brunthaler, A., Reid, M. J., Menten, K. M., Zheng, X. W., Moscadelli, L. & Xu, Y. (2009), this volume, (Paper V).

Burton, W. B. 1988, in "Galactic and Extragalactic Radio Astronomy (2^{nd} edition), eds. K. I. Kellermann & G. L Verschuur, " Springer-Verlag, Berlin and New York, p. 295-358

Dame, T. M., Hartmann, D. & Thaddeus, P. 2001, ApJ, 547, 792

Dehnen, W. & Binney, J. J. 1998, MNRAS, 298, 387

Fey, A. L. et al. 2004, AJ, 127, 3587

Georgelin, Y. M. & Georgelin, Y. P. 1976, A&A, 49, 57

Gerhard, O. 2002, *SSRv*, 100, 129

Hachisuka, K. et al. 2006, ApJ, 645, 337

Honma, M., Tamura, Y. & Reid, M. J. 2008, to appear in PASJ

Kobayashi, H. et al. 2005, in "Transits of Venus: New Views of the Solar System and Galaxy," Proceedings of IAU Colloquium No. 196, Ed. D.W. Kurtz. Cambridge: Cambridge University Press, p.496-496

Moscadelli, L., Menten, K. M., Walmsley, C. M. & Reid, M. J. 2002, ApJ, 564, 813

Moscadelli, L., Reid, M. J., Menten, K. M., Brunthaler, A., Zheng, X. W. & Xu, Y. (2009), this volume, (Paper II).

Oort, J. H., Kerr, F. J., Westerhout, G. 1958, MNRAS, 118, 379

Reid, M. J. 1993, ARA&A, 31, 345

Reid, M. J. & Brunthaler, A., 2004, ApJ, 616, 872

Reid, M. J., Readhead, A. C. S., Vermeulen, R. C. & Treuhaft, R. N., 1999, ApJ, 524, 816

Reid, M. J., Brunthaler, A., Menten, K. M., Moscadelli, L., Xu, Y., Zhang, B. & Zheng, X. W. (in preparation), Paper VI.

Taylor, J. H. & Cordes, J. M. 1993, ApJ, 411, 674

Walker, C. & Chatterjee, S., 2000, VLBA Scientific Memo 23, http://www.nrao.edu/memos/sci/gps_ion.html

Xu, Y., Reid, M. J., Zheng, X. W. & Menten, K. M. 2006a, *Science*, 311, 54

Xu, Y., Reid, M. J., Menten, K. M. & Zheng, X. W. 2006b, ApJS, 166, 526

Xu, Y., Reid, M. J., Menten, K. M., Brunthaler, A., Zheng, W. W. & Moscadelli, L. (2009), this volume, (Paper III).

Zhang, B., Zheng, X. W., Reid, M. J., Menten, K. M., Xu, Y., Moscadelli, L. & Brunthaler, A. (2009), this volume, (Paper IV).